Inorganic Chemistry
Cite This: Inorg. Chem. 2019, 58, 9368−9377
Article
pubs.acs.org/IC

Relationship between the Structure and Transport Properties in the $Ce_{1-x}La_xO_{2-x/2}$ System

Javier Zamudio-García,[†] José Manuel Porras-Vázquez,[†] Jesús Canales-Vázquez,[‡] Aurelio Cabeza,[†] Enrique R. Losilla,[†] and David Marrero-López*[,§]

[†]Departamento de Química Inorgánica and [§]Departamento de Física Aplicada I, Universidad de Málaga, 29071-Málaga, Spain
[‡]Renewable Energy Research Institute, University of Castilla-La Mancha, 02071 Albacete, Spain

Supporting Information

ABSTRACT: La-doped CeO_2 materials have been widely investigated for potential applications in different high-temperature electrochemical devices, such as fuel cells and ceramic membranes for hydrogen production. However, the crystal structure is still controversial, and different models based on fluorite, pyrochlore, and/or type-C structures have been considered, depending on the lanthanum content and synthesis method used. In this work, an exhaustive structural analysis of the $Ce_{1-x}La_xO_{2-x/2}$ system ($0.2 < x \leq 0.7$) is performed with different techniques. The average crystal structure, studied by conventional X-ray diffraction, could be considered to be a disordered fluorite; however, the local structure, examined by electron diffraction and Raman spectroscopy, reveals a biphasic mixture of fluorite and C-type phases. The thermal and electrical properties demonstrate that the materials with $x \geq 0.4$ are oxide ion proton conductors in an oxidizing atmosphere and mixed ionic electronic conductors in a reducing atmosphere. The water uptake and proton conductivity increase gradually with the increase in La content, suggesting that the formation of the C-type phase is responsible for the proton conduction in these materials.

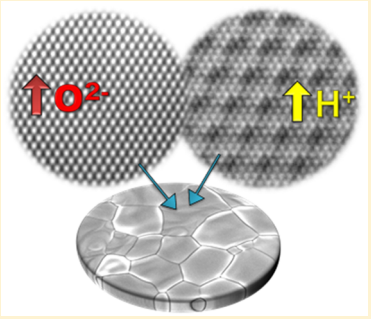

1. INTRODUCTION

La-doped CeO_2 materials are of great interest because of their numerous applications in different fields, including catalysis,[1−3] photoluminescence,[4,5] thermal barrier coatings, and electrochemistry.[6−8] In particular, these materials are widely used in high-temperature electrochemical devices for energy production and storage and as membranes for hydrogen production and solid oxide fuel cells because of their remarkable mixed ionic−electronic conductivity.[9−14]

The doping of CeO_2 with lower-valence cations, $Ce_{1-x}Ln_xO_{2-\delta}$ (Ln = Gd^{3+}, Sm^{3+}, and Y^3), creates oxygen vacancies in the lattice, leading to a significant enhancement in the ionic conductivity.[15−17] The total conductivity in this system depends on the nature and content of the dopant because they affect the degree of the lattice distortion, the number of crystalline defects, and the oxide ion mobility.[18,19] In general, the highest ionic conductivity is found for a critical dopant content of $0.1 < x < 0.2$, decreasing for higher concentrations. This behavior is attributed to the nonrandom distribution of the trivalent dopant and oxygen vacancies.[20] For high doping levels, a biphasic region formed by fluorite (e.g. $Fm\bar{3}m$) and C-type (e.g. $Ia\bar{3}$) phases has been observed, depending on the size mismatch between Ce^{4+} and the rare earth cation (Ln^{3+}).[21,22] The C-type structure is typical of rare earth sesquioxides A(i.e., Nd_2O_3, Pr_2O_3, etc.), where the high oxygen vacancy concentration leads to a rearrangement of the atoms in the crystal lattice, with respect to the ideal fluorite CeO_2, causing a doubling of the unit cell. This leads to two related phases (i.e., fluorite and C-type), where the diffraction peaks are overlapped, hindering their identification by conventional diffraction techniques.

In the $Ce_{1-x}La_xO_{2-x/2}$ system, the samples with low lanthanum content ($0 \leq x \leq 0.2$) are oxide ion conductors with an ideal fluorite-type structure.[23] The composition $Ce_{0.6}La_{0.4}O_{1.8}$ is also considered to be a fluorite and has been employed as an effective buffer interlayer to suppress the reaction and cation interdiffusion between $LaGaO_{3-\delta}$-based electrolytes and different SOFC electrode materials, including Ni-based anodes.[24,25] The composition with $x = 0.5$, initially reported as pyrochlore-type structure $La_2Ce_2O_7$,[26] exhibits high proton conductivity at low temperatures, and it has been investigated as a proton conductor for SOFCs and a membrane for hydrogen production.[27,28] However, there are many controversies regarding the real structure of this material from both density functional theory (DFT) calculations and neutron diffraction studies. Some authors reported that this material crystallizes with a pyrochlore-type structure, while others have suggested a disordered fluorite.[29−32] These discrepancies mostly arise from the different experimental techniques, the different synthesis methods used, and the thermal treatment of the materials, which control the chemical defects and consequently the crystal structure.

Despite the numerous technological applications of $Ce_{1-x}La_xO_{2-x/2}$ compounds, the structure and conductivity properties are not completely clear and require further

Received: April 16, 2019
Published: June 25, 2019

DOI: 10.1021/acs.inorgchem.9b01104
Inorg. Chem. 2019, 58, 9368−9377

investigation. The aim of this work is to offer a comprehensive study of the relationship between the structure and the electrochemical properties of $Ce_{1-x}La_xO_{2-x/2}$ ($0.2 \leq x \leq 0.7$) materials. A freeze-drying synthesis method is used to obtain fully dense ceramic pellets with an optimized microstructure and high electrical conductivity. The average structure is investigated as a function of La content by the Rietveld method of X-ray diffraction (XRD) at room temperature and high temperatures. The local order is examined for the first time by a combination of transmission electron microscopy (TEM) and μ-Raman. Finally, the electrochemical properties are studied by impedance spectroscopy in wet and dry gases and as a function of the oxygen partial pressure in order to obtain information on the bulk and specific grain boundary conductivity and the different ionic and electronic charge carriers.

2. EXPERIMENTAL SECTION

2.1. Synthesis. Powders with composition $Ce_{1-x}La_xO_{2-x/2}$ (x = 0.2, 0.4, 0.5, 0.6, and 0.7) were prepared by a freeze-drying precursor method similar to that reported elsewhere for related materials.[33] The starting reagents, $Ln(NO_3)_3{\cdot}6H_2O$ (Ln = Ce and La, 99.99%, Aldrich), were dissolved in distilled water in stoichiometric amounts. After that, ethylenediaminetetraacetic acid (EDTA, 99.99%, Aldrich) in a ligand to metal molar ratio of 1:1 was added as a complexing agent to stabilize the solution. The precursor solutions (concentration = 0.1 mol L^{-1} and pH 7) were frozen by dropwise addition into liquid nitrogen and then dehydrated by vacuum sublimation in a Scanvac Coolsafe freeze-dryer for 2 days. The dried precursors were first calcined at 300 °C for combustion and then at 800 °C for 1 h to remove the residual organic material.

The powders were compacted into disks of 10 and 1 mm diameter and thickness, respectively, under a pressure of approximately 100 MPa. The resulting pellets were placed on platinum plates, sintered at 1400 °C for 1 h, and cooled slowly at 5 °C min^{-1} to obtain an oxygen stoichiometry as close as possible to the equilibrium conditions at room temperature. All samples were prepared under identical experimental conditions to compare the structural properties. For the structural analysis, the pellets were finely grounded in an agate mortar.

2.2. Structural and Thermal Characterization. The crystal structure and phase purity were analyzed by high-resolution X-ray powder diffraction (XRD) on a X'Pert Pro PANalytical diffractometer with strictly monochromatic Cu $K\alpha_1$ radiation. High-temperature XRD data were recorded by using an Anton Paar HTK 1200 chamber in air from room temperature to 800 °C as described in detail elsewhere.[34] Phase identification and structural analysis were performed using the X'Pert HighScore Plus and GSAS programs.[35,36]

μ-Raman spectra were collected with a JASCO NRS-5100 Raman microscope by using an excitation line of 532 nm (Nd:YVO_4 laser), a power of 4.6 mW, a resolution of 2 cm^{-1}, and an acquisition time of 60 min.

The local structure was investigated by combining selected area electron diffraction (SAED) and high-resolution transmission electron microscopy (HRTEM) on a Jeol JEM-2100 instrument.

The microstructure and elemental composition of the ceramic pellets were examined with an FEI-SEM (Helios Nanolab) microscope equipped with an energy-dispersive X-ray spectrometer (EDX, X-Max Oxford). The average grain size was determined from the SEM micrographs and the linear intercept method.[37]

To investigate the possible water uptake in powder samples, thermogravimetric curves were recorded with an SDT Q600 (TA Instrument) from RT to 900 °C during the heating and cooling processes (5 °C·min^{-1}) under wet synthetic air (~2 vol % H_2O). The data were acquired in two different thermal cycles to test the reproducibility of the measurements.

2.3. Electrical Characterization. The electrical properties were investigated by impedance spectroscopy with a Solartron-1260 frequency response analyzer. The measurements were performed on cooling from 800 to 150 °C under dry and wet (2 vol % H_2O) air by flowing the gas through a desiccant and water bubbler, respectively, at a constant temperature of 20 °C. The drying system consisted of two consecutive glass columns filled with silica gel and molecular sieve beads (zeolite). The stabilization times were 15, 30, and 60 min at each measuring temperature to ensure that equilibrium was reached. The spectra were fitted with equivalent circuit models, using the ZView program to separate the bulk and grain boundary resistance contributions to the total conductivity. Pt ink and meshes were used as current collectors. Moreover, the conductivity was determined as a function of the oxygen partial pressure (pO_2) to identify the ionic and electronic charge carriers. For this purpose, the pellet were reduced in a closed tube furnace cell with dry 5% H_2–Ar at 700 °C for 12 h, reaching a minimum in oxygen activity inside the furnace to ensure that the sample was close to equilibrium. Then, the gas flow was switched off and pO_2 slowly recovered to atmospheric pressure by free diffusion because the system is not fully airtight. The impedance spectra were collected during the reoxidation process (~2 days), and the oxygen partial pressure was measured with an YSZ oxygen sensor. The structure and microstructure of the samples after the electrochemical characterization were studied by XRD and SEM, respectively, and no evidence of degradation was observed.

3. RESULTS AND DISCUSSION

3.1. Average Structure and Thermal Characterization. XRD patterns show that samples with lanthanum content $x \leq$ 0.6 are single phases (Figure 1). Beyond this composition,

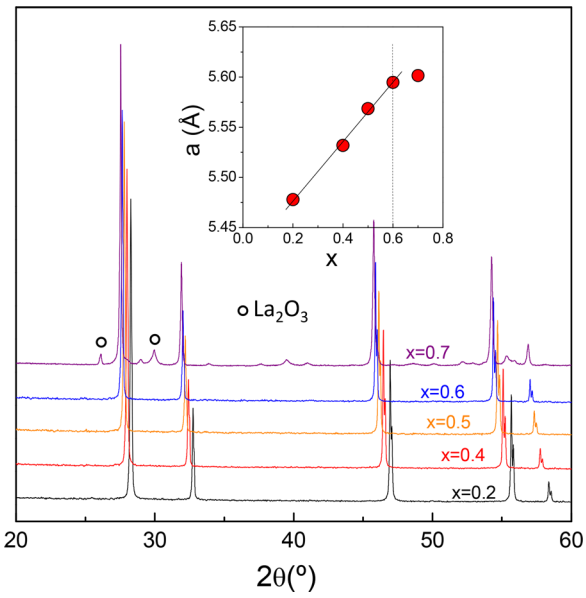

Figure 1. X-ray diffraction patterns of the $Ce_{1-x}La_xO_{2-x/2}$ ($0.2 \leq x \leq$ 0.7) series synthesized from freeze-dried powders at 1400 °C for 1 h. Additional diffraction peaks assigned to La_2O_3 impurities are observed for $x \geq 0.7$. The inset figure shows the evolution of the lattice cell parameter as a function of La content.

diffraction peaks assigned to La_2O_3 are observed, indicating that the lanthanum solubility in CeO_2 is approximately x = 0.6. The unit cell parameter follows a linear dependence up to x = 0.6, confirming the existence of a solid solution, and beyond this composition, the unit cell parameters remain invariable (inset of Figure 1). It has to be noticed that this solubility limit is higher than that reported by Andrievskaya et al., where La_2O_3 secondary phases were detected by both XRD and SEM analysis for compositions with $x \geq 0.5$.[38] This discrepancy might be explained by the different synthesis method as well as

DOI: 10.1021/acs.inorgchem.9b01104
Inorg. Chem. 2019, 58, 9368–9377

the different thermal treatment used because the specimens prepared in the present study are obtained at much lower temperatures and shorter sintering times (i.e., 1400 °C for 1 h compared to 1500 °C for 150 h by Andrievskaya et al.[38]).

The average crystallographic structure of the materials with $x \leq 0.5$, analyzed by the Rietveld method, can be considered to be a disordered fluorite (e.g., $Fm\bar{3}m$) because additional diffraction peaks assigned to superstructure ordering are not observed (Figure 2a), even for $x = 0.5$, which has been

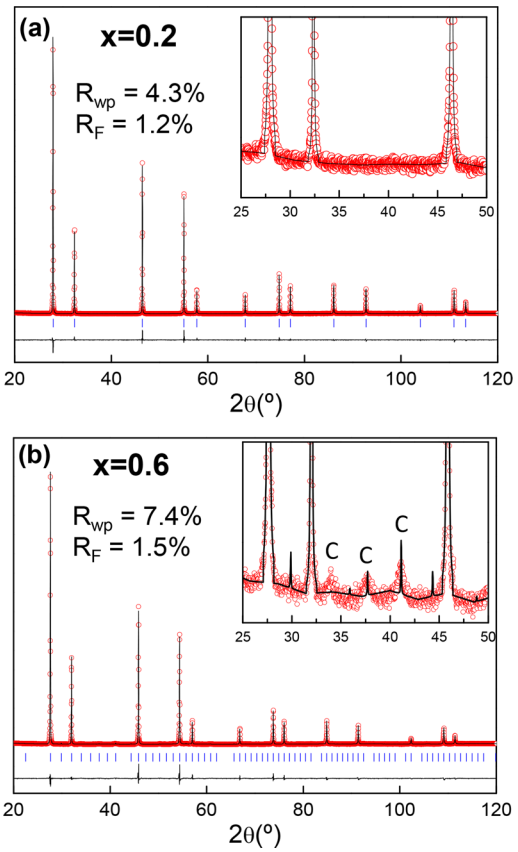

Figure 2. Rietveld plots of (a) $Ce_{0.8}La_{0.2}O_{1.9}$ and (b) $Ce_{0.4}La_{0.6}O_{1.7}$ refined by considering a disordered fluorite (e.g., $Fm\bar{3}m$) and a C-type (e.g., $Ia\bar{3}$) structure, respectively. The diffraction peaks ascribed to the C-type superstructure are indicated in the inset of (b).

considered to be a pyrochlore-type phase ($La_2Ce_2O_7$).[26] As commented on in the Introduction, the precise structure of $La_2Ce_2O_7$ is still unclear, and contradictory results are reported in the literature.[29−32] For instance, Yamamura et al. reported that the structure of $Ln_2Ce_2O_7$ (Ln = La^{3+}, Nd^{3+}, Sm^{3+}, Gd^{3+}, Y^{3+}, Eu^{3+}, and Yb^{3+}) depends on the ionic radii of the trivalent rare earth cation. When $r(Ln^{3+})/r(Ce^{4+}) < 1.17$, a C-type phase is stabilized;[39] however, $r(La^{3+})/r(Ce^{4+}) = 1.3$ for $La_2Ce_2O_7$, suggesting the formation of a disordered-fluorite phase. In accordance with this study, neutron diffraction and X-ray absorption have revealed that $La_2Ce_2O_7$ forms a fully disordered fluorite.[31] On the contrary, Kalland et al. investigated this compound by neutron diffraction, and no superstructure peaks were detected. However, the diffuse scattering and background modulation indicated that the local structure deviates from that of ideal fluorite, suggesting that there is a short-range order consistent with a C-type phase. Artini et al. have reported a biphasic mixture in Sm- and Gd-doped CeO_2 by synchrotron X-ray diffraction, where the C-type microdomains are embedded in the fluorite matrix.[21] It should be noted that the Ln_2O_3−CeO_2 (Ln = Nd, Sm, Gd, Y, etc.) system forms a solid solution over the whole compositional range from fluorite (CeO_2) to the C-type phase (Ln_2O_3); therefore, biphasic mixtures are formed for the intermediate compositions.[21,22] However, in the case of $Ce_{1-x}La_xO_{2-x/2}$, a solid solution exists for $x \leq 0.6$, and above this composition, La_2O_3 with hexagonal structure (e.g., $P\bar{3}m1$) is segregated. Thus, a different structural evolution for La doping is expected for this system, which has not yet been investigated.

In the present study, the composition with $x = 0.6$, which has not been reported in the literature, shows additional diffraction peaks in the XRD pattern that are similar to those observed for a C-type superstructure (Figure 2b). However, the Rietveld refinement, considering a single C-type phase (e.g., $Ia\bar{3}$), is not adequate to fit the pattern because of anomalous peak broadening. This leads to relatively high agreement factors, $R_{wp} = 7.2\%$, when compared to those samples with low La doping, $R_{wp} = 4.2\%$ for $x = 0.2$. Similar behavior was previously observed for Y-doped CeO_2, which was attributed to a biphasic mixture of fluorite and C-type phases.[41]

The superstructure peaks become more intense for composition $x = 0.7$, despite the fact that this material shows secondary phases of La_2O_3, suggesting a higher amount of the C-type phase with increasing La content (Figure S1, Supporting Information). All of these findings seem to indicate that samples with high La content are a mixture of fluorite and C-type phases, similar to those observed for Nd-, Gd-, and Sm-doped CeO_2.[21,40]

High-temperature XRD patterns for the sample with the lowest La content ($x = 0.2$) show fluorite structure over the whole temperature range studied (RT−800 °C) (Figure S2a). The lattice cell parameter increases linearly with temperature, following the expected behavior (Figure 3a). Composition $x = 0.4$ may also be considered to be a fluorite phase over the whole temperature range (Figure S2b); however, the lattice cell parameters deviate slightly from a linear trend at low temperatures ($T < 300$ °C). In the case of the sample with $x = 0.6$, diffraction peak broadening is observed at low temperatures and high 2θ values, indicating the presence of two fluorite-related phases. However, superstructure reflections associated with the C-type phase are not observed, possibly because of the low resolution of XRD data (Figure S2c). The peak broadening decreases gradually with the increase in temperature so that only one fluorite-type phase is observed at 400 °C. It has to be noticed that the measurements are reproducible upon heating and cooling processes. For this sample, an average unit cell parameter was estimated by considering a single cubic fluorite over the whole temperature range. The variation of the unit cell parameter with the temperature shows a sudden shrinkage at ∼300 °C, and above this temperature, a linear thermal expansion is observed.

Thermogravimetric measurements were performed in humidified air to elucidate the origin of this anomalous thermal expansion of the unit cell. The TG curves show a mass increase below 400 °C during the cooling process, which is more important as the La content increases (Figure 3b). This behavior might be attributed to water uptake, according to the hydration of oxygen vacancies with the consequent formation of protonic defects:[13]

DOI: 10.1021/acs.inorgchem.9b01104
Inorg. Chem. 2019, 58, 9368−9377

$$H_2O(g) + O_O^x + V_O^{\bullet\bullet} \rightarrow 2OH_O^{\bullet} \quad (1)$$

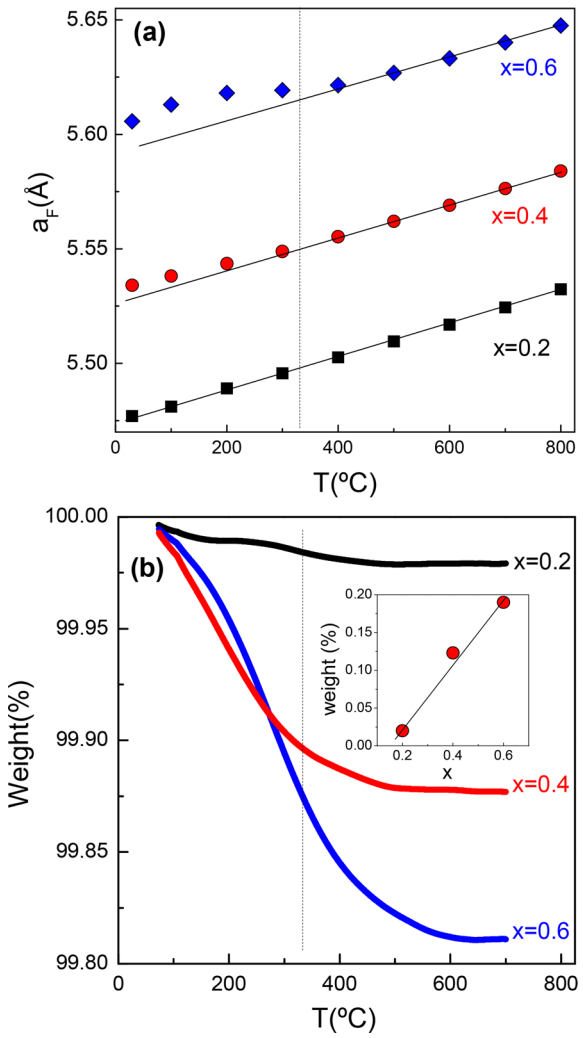

Figure 3. (a) Variation of the lattice cell parameter with temperature and (b) thermogravimetric curves of $Ce_{1-x}La_xO_{2-x/2}$ materials collected under humidified air upon cooling. The inset of (b) shows the weight uptake as a function of La content.

Similar results were previously reported for proton ceramic conductors based on lanthanum molybdates, where the water uptake also leads to a chemical expansion of the unit cell volume.[42]

The water uptake is negligible for samples with low La content ($x = 0.2$) and a single fluorite-type structure; however, it is significant for those with high La content ($x \geq 0.4$), which could possibly be a mixture of fluorite and C-type phases. These findings suggest that only the C-type phase is hydrated, corroborated by the fact that the highest water adsorption is for $x = 0.6$. Thus, there is a clear relationship between the water uptake and the unit cell expansion at low temperature. On the other hand, the low water uptake in samples with a fluorite phase suggests that these are poor proton conductors. In contrast, the formation of the C-type phase seems to enhance the water adsorption, which may also lead to an improvement in the proton conductivity.

The thermal expansion coefficients at high temperature, determined from XRD data, decrease slightly with increasing La content from 13.5×10^{-6} K^{-1} for $x = 0.2$ to 12.0×10^{-6} K^{-1} for $x = 0.6$ and are in agreement with those reported in the literature.[43]

3.2. Structural Analysis by TEM. Selected-area electron diffraction (SAED) patterns are obtained for all the samples along the main zone axes and different crystals (Figure 4). For simplicity, all of the patterns are indexed by considering a simple cubic fluorite; however, additional reflections, related to superstructure ordering, are observed in samples with high La content.

The composition with the lowest La content ($x = 0.2$) shows only characteristic reflections of a cubic disordered fluorite structure (e.g., $Fm\bar{3}m$) with a lattice cell parameter of $a_F = 5.5$ Å (Figure 4a–d). For $x = 0.4$ and 0.5, additional reflections are observed along the (200) and (020) directions, indicating the formation of a 2×2 fluorite supercell consistent with the C-type phase; however, these superstructure reflections are not observed in other zone axes (Figure S3). As the La content increases, diffuse scattering is observed along the (220) direction, and its intensity increases gradually, leading to a superlattice in which the (220) plane spacing of the fluorite is apparently quadrupled (Figure 4g,h). Similar behavior has been observed in other doped CeO_2 solid solutions. For

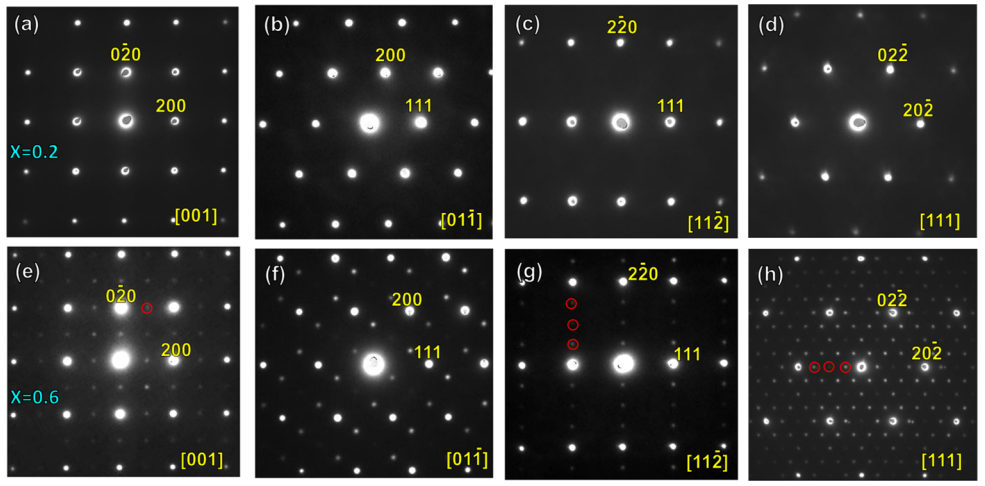

Figure 4. SAED patterns of (a–d) $Ce_{0.8}La_{0.2}O_{1.9}$ and (e–h) $Ce_{0.4}La_{0.6}O_{1.7}$ in different zone axes. The patterns are indexed by considering a single cubic fluorite-type structure. Weak reflections assigned to the C-type superstructure are observed for $Ce_{0.4}La_{0.6}O_{1.7}$.

DOI: 10.1021/acs.inorgchem.9b01104
Inorg. Chem. 2019, 58, 9368–9377

instance, Wallenberg et al. studied the CeO_2−Y_2O_3 system by electron diffraction, and they observed a superstructure with quadrupled (220) when the Y_2O_3 content is higher than 60 mol %.[44] The results suggested the formation of a C-type Ln_2O_3 compound (e.g., $Ia\bar{3}$), with ordered oxygen vacancies along the (220) direction, as the origin of the additional superlattice reflections. It has to be noticed that superstructure spots 1/4 (220) are not allowed in the $Fm\bar{3}m$ and $Ia\bar{3}$ space groups, so they are associated with double diffraction.[44]

HRTEM images confirm further that the samples with low La content (x = 0.2) are disordered fluorites without the visible formation of ordered defects, not even clusters. The calculated structure is in good agreement with the experimental image in different zone axes (Figure 5a,b). In the case of the samples

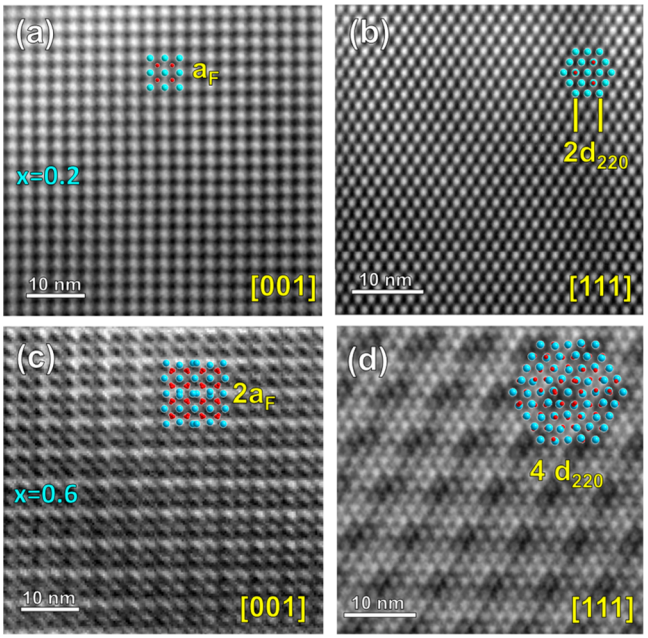

Figure 5. HRTEM image of (a, b) $Ce_{0.8}La_{0.2}O_{1.9}$ and (c, d) $Ce_{0.4}La_{0.6}O_{1.7}$ in the [001] and [111] zone axes. Simulated images of the disordered fluorite and the 2 × 2 C-type superstructure are included.

with the highest La content (x = 0.6), a new periodicity is observed in which the lattice parameter is doubled compared to that of the parent fluorite (Figure 5c,d). The simulated image, considering a C-type structure with cell parameter a_c = $2a_F$ = 11.0 Å and space group $Ia\bar{3}$, shows a good match with the experimental image. For intermediate compositions x = 0.4 and 0.5, diffuse scattering and microdomains without and with superstructure reflections are observed in the crystals, indicating a mixture of fluorite and C-type structures (Figure S4).

3.3. μ-Raman Characterization. The samples are studied with Raman spectroscopy in order to further confirm the presence of mixed-fluorite and C-type phases because this technique is highly sensitive to the identification of the formation of oxygen vacancies and differences in oxygen atomic positions in the lattice after La doping. An undoped sample of CeO_2 is included for comparison purposes. The spectra show different bands corresponding to fluorite- and C-type structures, depending on the La content (Figure 6).

Undoped ceria exhibits only a sharp single peak at 465 cm^{-1}, assigned to the F_{2g} symmetrical stretching vibrational mode of

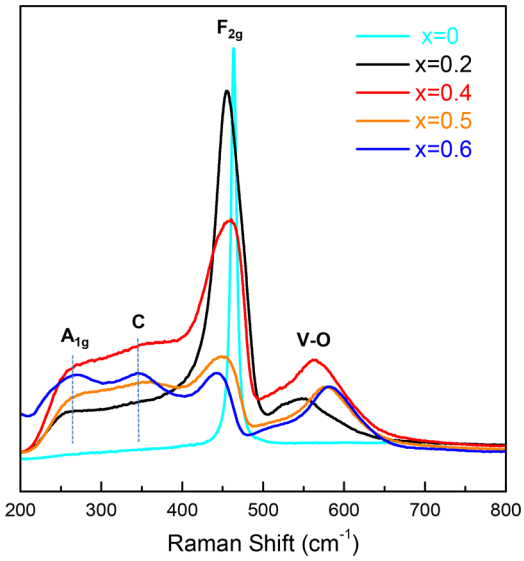

Figure 6. Raman spectra of the $Ce_{1-x}La_xO_{2-x/2}$ series collected at room temperature.

the Ce−O bond in 8-fold coordination.[45] This signal broadens, drops in intensity, and becomes progressively asymmetric as the La content increases as a result of the loss of translational symmetry with the introduction of defects and anion vacancies into the lattice. All La-doped samples show an asymmetric band located between 540 and 580 cm^{-1}, formed by two overlapped contributions, whose relative intensity changes progressively with the increase in La content. The first contribution at 540 cm^{-1} is assigned to the interaction between oxygen vacancies and the six neighboring oxygens (V−O).[46−48] The origin of the second contribution has been differently interpreted in the literature with respect to the presence of oxygen vacancies due to Ce^{4+} to Ce^{3+} reduction or oxygen nonstoichiometry due to the thermal treatment of the samples.[22] However, undoped CeO_2 does not show this contribution, proving that La-doped samples do not present any appreciable oxygen depletion. Therefore, the signal at 580 cm^{-1} has an intrinsic nature possibly because of the gradual phase transformation from a fluorite to a C-type phase.

The band observed at 260 cm^{-1} (A_{1g}) is consistent with that observed by Nakajima et al. in Y-doped CeO_2, which they associated with oxygen vacancy formation.[48]

From x = 0.4, a new signal arises at 350 cm^{-1}, which is assigned to the C-type structure, produced by the symmetrical stretching vibrational mode of Ce−O in 6-fold coordination.[47] The relative intensity of I_{F2g}/I_{V-O} signals decreases significantly with increasing La content as a result of the gradual phase transformation from a fluorite to a C-type phase. Similar results were previously reported for doped CeO_2 with smaller rare earth cations, such as Sm, Gd, and Nd.[21,49,50] These findings further show a biphasic mixture where the amount of the C-type phase grows from x = 0.4, corroborating the XRD, electron diffraction, and thermogravimetric measurements. On the other hand, it is also worth noting that the presence of C-type domains within the fluorite structure has significant effects on the oxide ion and proton conductivity of the materials, which will be treated in the following section.

3.4. Microstructural and Electrical Characterization. The SEM images demonstrate that all samples exhibit high densification with relative densities above 98% (Figure S5).

DOI: 10.1021/acs.inorgchem.9b01104
Inorg. Chem. 2019, 58, 9368−9377

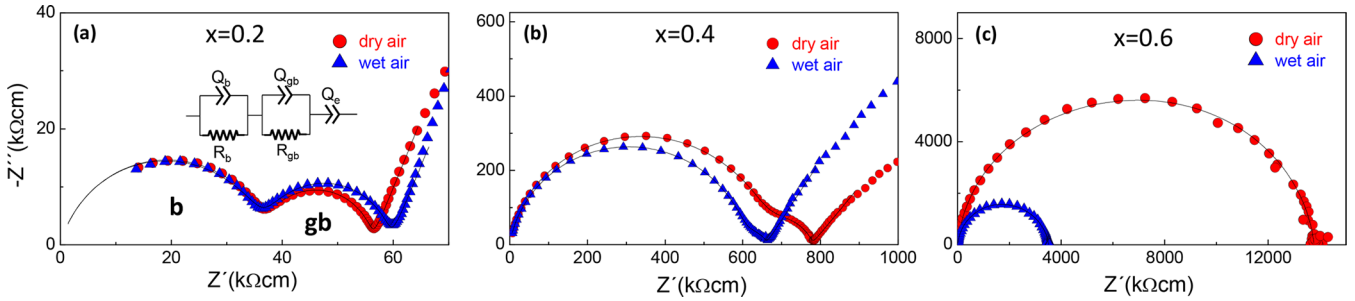

Figure 7. Impedance spectra of $Ce_{1-x}La_xO_{2-x/2}$: (a) $x = 0.2$, (b) $x = 0.4$, and (c) $x = 0.6$ in dry and wet air at 250 °C. The inset in (a) shows the equivalent circuit used to fit the data.

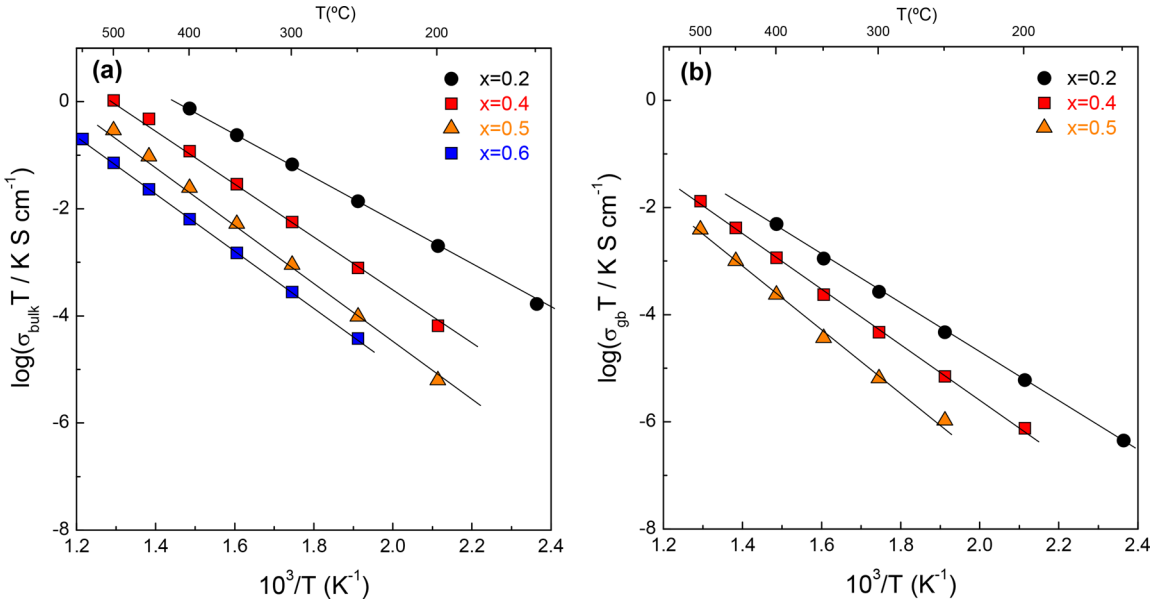

Figure 8. Arrhenius plots of the (a) bulk and (b) specific grain-boundary conductivity of $Ce_{1-x}La_xO_{2-x/2}$.

The EDX mapping analysis reveals a homogeneous distribution of the elements with a nominal composition similar to that of the theoretical one for $x \leq 0.6$. In contrast, samples with composition $x > 0.6$ show lanthanum oxide segregation, which is preferentially located on the pellet surface (Figure S4e). This sample is mechanically unstable after exposure to air for several days as a result of carbonation and hydration; therefore, it is not electrically characterized. The rest of the samples are stable after annealing in air for months.

The average grain size of the pellets increases exponentially with the La content from 0.6 μm for $x = 0.2$ to 3.0 μm for $x = 0.6$ (Figure S5f). This behavior is usually attributed to enhanced diffusion at the grain boundary during the sintering process due to the existence of a dopant concentration gradient between the grain interior and the grain boundary region, which decreases for those samples with high dopant content, in agreement with the space−charge model, improving the grain growth rate.[51]

The impedance spectra at low temperature ($T < 500$ °C) are composed of three different contributions, assigned to the grain-interior, grain-boundary, and electrode processes at the ceramic/Pt interface (Figure 7). At higher temperatures, the electrolyte contributions appear above the limit of detection of the equipment, and only the total conductivity and the sum of the bulk and grain-boundary resistances are determined.

The spectra are analyzed by an equivalent circuit formed by serial (RQ) elements (inset of Figure 7a). Thus, the resistance R_i and pseudocapacitance Q_i of the bulk and grain boundary contributions are determined. These parameters are used to calculate the capacitances C_i from the following relation:[52,53]

$$C = \frac{(R_i Q_i)^{1/n_i}}{R} \tag{2}$$

These take typical values of ~5 pF·cm^{-1}, 5 nF·cm^{-1}, and 1 mF·cm^2 for the bulk, grain-boundary, and electrodes processes, respectively.[54]

The impedance spectra clearly show that the bulk resistance increases significantly with increasing La content, which is usually explained by the high concentration of oxygen vacancies in the lattice and the stronger interaction between the ionic carriers and the trivalent dopant, in addition to the gradual phase transformation from disordered fluorite to ordered C-type that causes a significant reduction of the oxygen vacancy mobility.[55−57] On the other hand, the samples with high La content exhibit lower bulk resistance in wet air than in dry air, indicating the presence of proton conduction at low temperature. These results are consistent with the thermogravimetric analysis of Figure 3b, where the water uptake increases progressively for samples with higher La content.

DOI: 10.1021/acs.inorgchem.9b01104
Inorg. Chem. 2019, 58, 9368−9377

The Arrhenius plots of the bulk conductivity for samples with different La content are shown in Figure 8. It is well known that the bulk conductivity in doped CeO_2 depends on the ionic radii of the dopant and its content. In particular, the ionic radius of La^{3+} (1.16 Å) is higher than that of Ce^{4+} (0.97 Å), leading to a large lattice distortion that consequently reduces the oxide ion mobility. In general, for low doping levels ($x < 0.2$), the highest values of ionic conductivity are found for Gd^{3+} (1.053 Å) and Sm^{3+} (1.079 Å), minimizing the changes in the lattice parameters of pure CeO_2.[57] In addition, the increase in La content results in the gradual formation of the C-type phase, with ordered oxygen vacancies and thus lower mobility, leading to a significant reduction in the oxide ion conductivity. The increase in the activation energy from 0.84 eV for $x = 0.2$ to 1.12 eV for $x = 0.6$ constitutes further evidence of the negative effect of high La content on the bulk conductivity (Table 1).

Table 1. Conductivity Data for the $Ce_{1-x}La_xO_{2-x/2}$ Series in a Dry Air Atmosphere and Estimated Ionic Transport Numbers t_i at 700 °C and $pO_2 = 10^{-22}$ atm

x	σ_{bulk} (μS/cm) 250 °C	σ_{gb} (nS/cm) 250 °C	E_{bulk} (eV)	E_{gb} (eV)	σ_{total} (mS/cm) 700 °C	δ_{gb} (nm)	t_i
0.2	27.00	90.0	0.84	0.91	27.0	1.1	0.43
0.4	1.51	13.5	1.02	1.03	14.0	1.56	0.32
0.5	0.18	2.0	1.12	1.15	7.2	1.42	
0.6	0.08		1.12		2.4		0.35

In the case of the grain boundary contribution, the ratio of the grain boundary to the bulk resistance decreases with increasing La content, a phenomenon usually associated with the large grain size of the ceramic pellets as well as a scavenger effect (Figure 7).[57] The brick-layer model is used to determine the specific grain boundary conductivity σ_{gb} by assuming similar dielectric constants ($\varepsilon_r = 30$) for the bulk and grain boundary regions[52,53]

$$\sigma_{gb} = \frac{\varepsilon_o \varepsilon_r}{C_{gb} R_{gb}} \tag{3}$$

where R_{gb} and C_{gb} are the grain boundary resistance and capacitance, respectively, and ε_o is the vacuum electrical permittivity.

The grain boundary conductivity is 2 orders of magnitude inferior to those of the grain interior and decreases with La doping, similar to the bulk conductivity (Figure 8). Regarding the values of the activation energy, they are somewhat higher than those of the bulk, increasing from 0.91 eV for $x = 0.2$ to 1.15 eV for $x = 0.6$ (Table 1). In the case of the sample with $x = 0.6$, the grain boundary contribution is not observed, and the corresponding conductivity is not determined (Figure 7c).

The grain boundary width δ_{gb} is estimated from the thickness L, surface area S, and average grain size D of the ceramic pellets as follows:[52,53]

$$\delta_{gb} = \frac{\varepsilon_o \varepsilon_r}{C_{gb}} \frac{DS}{L} \tag{4}$$

The grain boundary widths are comparable for the different samples, varying between 1.1 and 1.5 nm (Table 1). One should notice that δ_{gb} has been estimated by assuming similar permittivity values for the bulk and the grain interior region, although their compositions might be different. Thus, the main differences between the grain boundary properties correspond mainly to changes in the conductivity rather than differences in the dielectric constant; however, the obtained values are rather reasonable when compared to those previously reported for $Ce_{0.8}Gd_{0.2}O_{1.9}$ (i.e., 1 to 2 nm[57]), confirming that the brick-layer model is adequate for describing the grain boundary conduction in these materials.

Arrhenius plots of the total conductivity are shown in Figure 9. As expected, samples with higher La contents exhibit lower

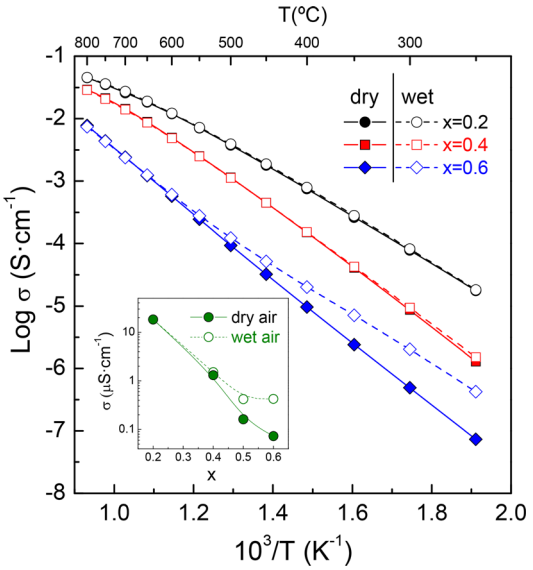

Figure 9. Total conductivity of $Ce_{1-x}La_xO_{2-x/2}$ in dry and wet air. The inset shows the variation in the conductivity as a function of the La content in dry and wet air at 250 °C.

conductivity, especially in the low-temperature range with differences of up to 2 orders of magnitude. In the high-temperature range, the interaction between oxygen vacancy charge carriers and the trivalent dopant decreases; consequently, the conductivity differences are reduced.[55,56]

The samples with low La content ($x = 0.2$) exhibit the same conductivity under dry and wet atmospheres, indicating negligible proton conductivity. Previous studies for low-doped CeO_2 confirmed that $Ce_{0.8}Yb_{0.2}O_{1.9}$ exhibits the highest proton conductivity among these materials, with a rather low value of 1 μS cm^{-1} at 700 °C.[58] It must be mentioned that the C-type structure in the Ln_2O_3–CeO_2 system tends to be stabilized as the ionic radii of Ln^{3+} decreases; therefore, a significant amount of the C-type phase in Yb-doped samples might explain the improved proton conductivity. Some other authors have reported proton conductivity in nanocrystalline low-doped ceria at low temperature;[59,60] however, recent studies have confirmed that this contribution is associated with a superficial proton conduction instead of volumetric proton conductivity, where the transport under wet conditions is limited to the sample surface.[61]

Samples with lanthanum content $x \geq 0.5$ show a significant improvement in conductivity in wet air, attributed to proton conduction at low temperatures (inset of Figure 9). It is also worth noting that the proton conductivity for $x = 0.6$ is superior to that of $x = 0.5$, which is related to an increase in the amount of the C-type phase and the water uptake. The proton transport numbers, estimated from the conductivity values in wet and dry air, are about 0.62 and 0.89 for $x = 0.5$ and 0.6,

DOI: 10.1021/acs.inorgchem.9b01104
Inorg. Chem. 2019, 58, 9368–9377

respectively, at 250 °C. These values are only an estimation, thus additional measurements, such as electromotive force under a water partial pressure gradient, are needed to obtain precise values of the proton transport numbers, which are presumably higher than those given here. The proton transport number decreases abruptly to 0.24 at 500 °C, a temperature at which water uptake is not observed by thermogravimetric analysis and the materials are predominantly oxide ion conductors. In the case of the sample with x = 0.4, the structural analysis revealed that this is composed of a mixture of fluorite and C-type phases. However, the volume fraction of the C-type phase is not large enough to ensure percolation, so the proton conduction is not significant (i.e., 8.5 and 9.5 μS cm^{-1} in dry and wet air, respectively, at 250 °C).

It has to be noticed that the values of the total conductivity, obtained in the present work, are comparable or even higher than those previously reported, possibly because of the higher densification of the samples as well as the lower sintering temperature and shorter time used in the preparation. For instance, the conductivity for x = 0.5 is 7.2 mS cm^{-1} at 700 °C, which is somewhat higher than those previously reported for the same composition (e.g., 5.0 and 4.0 mS cm^{-1}).[27,14]

In reducing atmospheres, CeO_2-based materials are expected to exhibit n-type electronic conductivity due to a partial reduction of Ce^{4+} to Ce^{3+}. Hence, to evaluate the effect of La doping on the electronic conductivity, the impedance spectra were acquired as a function of the oxygen partial pressure (pO_2) between air (0.21 atm) and very reducing conditions (10^{-25} atm, Figure 10). The conductivity is independent of

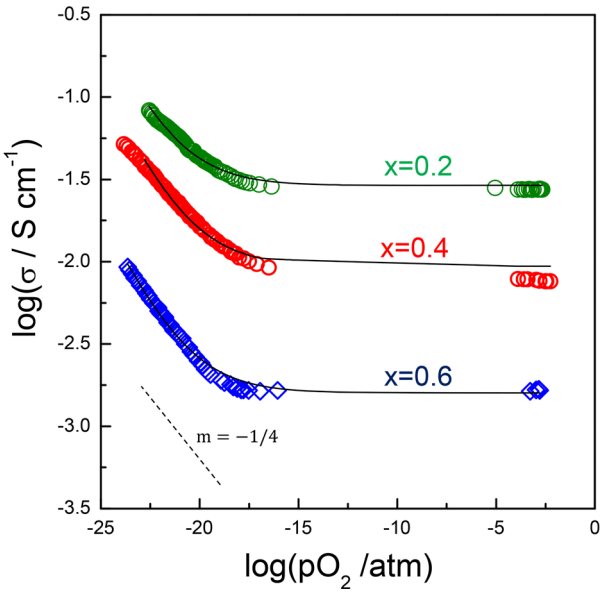

Figure 10. Dependence of the conductivity of $Ce_{1-x}La_xO_{2-x/2}$ on the oxygen partial pressure at 700 °C.

pO_2 in the range of 10^{-17}–0.21 atm, indicating a predominant oxide ion conduction under moderate reducing conditions. At lower values of pO_2, Ce^{4+} is partially reduced to Ce^{3+}, which leads to n-type electronic conductivity according to the following relation[62]

$$O_O^x + 2C_{Ce}^x \rightarrow \frac{1}{2}O_2(g) + V_O^{\bullet\bullet} + 2Ce'_{Ce} \quad (5)$$

Thus, the total conductivity can be expressed by the classical approach, assuming that the proton contribution is negligible at high temperature

$$\sigma = \sigma_i + \sigma_n^o \cdot (pO_2)^m \quad (6)$$

where σ_i and σ_n^o are the ionic and partial n-type electronic conductivities, respectively, at pO_2 = 1 atm and m is an exponent whose sign and magnitude provide an indication of the rate-controlling species and defects.

The fitting results are given in Figure 10, and all samples follow the same power law dependence with m = 1/4. The ionic transport numbers at 700 °C and $pO_2 = 10^{-22}$ atm vary between 0.43 for x = 0.2 and 0.35 for x = 0.6 (Table 1). In general, samples with high La content seem to exhibit somewhat lower ionic transport numbers because of a significant reduction in the oxide ion conductivity compared to the electronic one. This also explains the low open circuit voltage obtained for SOFCs based on $La_2Ce_2O_7$ electrolytes (e.g., about 0.8 V at 600 °C).[26,63] It should be noticed that these ionic transport numbers are much lower than those obtained under real fuel cell conditions under an oxygen chemical potential gradient.[14] Hence, the potential application of these electrolytes in SOFC technology is limited to the intermediate temperature range (400–700 °C), where the electrolytic domain is predominant. However, the high ambipolar conductivity makes these materials more attractive for high-temperature hydrogen membranes because the values of proton conductivity are comparable to those of traditional doped $SrCeO_{3-\delta}$ and $La_{6-x}WO_{12-\delta}$ proton conductors.[13,33] However, the transport numbers of the different charge carriers should be determined to evaluate the potential application of these materials.

Finally, a structural study at high temperature is highly demanded to better understand the conductivity properties by considering that these materials are a biphasic mixture of fluorite and C-type. Structural characterization at high temperature by synchrotron X-ray radiation and neutron diffraction is ongoing to clarify this point. In addition, the proton-conducting properties in other compositions of the Ln_2O_3–CeO_2 system with C-type structure, such as Nd, Sm, Y, and Gd, should be investigated.

CONCLUSIONS

The structure and electrical properties of the $Ce_{1-x}La_xO_{2-x/2}$ series were studied in the solid solution range ($x \leq 0.6$). A gradual phase transformation from a disordered fluorite to a C-type structure was observed by both electron diffraction and Raman spectroscopy. Samples with low La content ($x \leq 0.2$) are apparently disordered fluorites without visible oxygen vacancy ordering; however, for $x \geq 0.4$, superstructure and diffuse scattering reflections were observed in the electron diffraction patterns, consistent with the formation of C-type domains within the fluorite crystals.

The oxide ion conductivity decreased with increasing La content as a result of the different mismatch between the ionic radii of Ce^{4+} and La^{3+}, which produces a larger distortion in the unit cell. In addition, the formation of C-type superstructure domains with ordered oxygen vacancies further limits the oxide ion mobility.

Significant water uptake was observed by thermogravimetric analysis for $x \geq 0.4$. Above this composition, the C-type domains percolate through the crystals, leading to significant proton conductivity at low temperature, reaching a maximum

DOI: 10.1021/acs.inorgchem.9b01104
Inorg. Chem. 2019, 58, 9368–9377

for x = 0.6. The estimated proton transport numbers increase with La content from 0.62 for x = 0.5 to 0.89 for x = 0.6 at 250 °C. In reducing atmospheres, all materials are mixed oxide−electron conductors with similar ionic transport numbers.

■ ASSOCIATED CONTENT

Supporting Information

The Supporting Information is available free of charge on the ACS Publications website at DOI: 10.1021/acs.inorgchem.9b01104.

Additional experimental results, including an XRD Rietveld plot for x = 0.7; selected region of high-temperature XRD patterns; SAED patterns and HRTEM image for x = 0.4 and 0.5; and SEM image and average grain size of the ceramic pellets (PDF)

■ AUTHOR INFORMATION

Corresponding Author

*E-mail: marrero@uma.es. Tel: +34 952137057. Fax: +34 952132382.

ORCID

José Manuel Porras-Vázquez: 0000-0002-2673-1413
Jesús Canales-Vázquez: 0000-0003-4089-2034
Aurelio Cabeza: 0000-0002-1582-3240
Enrique R. Losilla: 0000-0002-3361-2340
David Marrero-López: 0000-0003-0632-6442

Notes

The authors declare no competing financial interest.

■ ACKNOWLEDGMENTS

This work was supported by MINECO through the RTI2018-093735-B-I00 and MAT2016-77648-R research grants (Spain), cofunded by FEDER. J.M.P.-V. thanks the University of Málaga for funding. J.Z.-G. thanks the Spanish Ministry of Education, Culture and Sport for an FPU grant (FPU17/02621).

■ REFERENCES

(1) Xu, J.; Zhang, Y.; Liu, Y.; Fang, X.; Xu, X.; Liu, W.; Zheng, R.; Wang, X. Optimizing the Reaction Performance of $La_2Ce_2O_7$-Based Catalysts for Oxidative Coupling of Methane (OCM) at Lower Temperature by Lattice Doping with Ca Cations. *Eur. J. Inor. Chem.* **2019**, *2*, 183−194.

(2) Ayawanna, J.; Sato, K. Photoelectrodeposition effect of lanthanum oxide-modified ceria particles on the removal of lead (II) ions from water. *Catal. Today* **2019**, *321*−*322*, 128−134.

(3) Liu, F.; Zhao, L.; Wang, H.; Bai, X.; Liu, Y. Study on the preparation of Ni-La-Ce oxide catalyst for steam reforming of ethanol. *Int. J. Hydrogen Energy* **2014**, *39*, 10454−10466.

(4) Shi, S.; Yang, Y.; Guo, P.; Wang, J.; Geng, L.; Fu, L. Improved morphology and optimized luminescence of Eu^{3+}-doped $La_2Ce_2O_7$ composite nanopowders by surfactant-assisted solution combustion synthesis. *J. Lumin.* **2019**, *206*, 91−96.

(5) Deus, R. C.; Cortés, J. A.; Ramirez, M. A.; Ponce, M. A.; Andres, J.; Rocha, L. S. R.; Longo, E.; Simões, A. Z. Photoluminescence properties of cerium oxide nanoparticles as a function of lanthanum content. *Mater. Res. Bull.* **2015**, *70*, 416−423.

(6) Liu, K.; Bai, Y.; Kang, Y. X.; Zhang, L.; Tang, J. J.; Wang, Y.; Li, J. R.; Cheng, H. Y.; Fan, W.; Li, B. Q.; Song, X. L. Investigation of particle characteristics, composition and microstructure of $La_xCe_{1-x}O_{2-x/2}$ thermal barrier coatings during supersonic atmospheric plasma spray using Box−Behnken design. *Surf. Coat. Technol.* **2016**, *286*, 9−15.

(7) Cao, X.; Vassen, R.; Fischer, W.; Tietz, F.; Jungen, W.; Stöver, D. Lanthanum-cerium oxide as a thermal barrier-coating material for high-temperature applications. *Adv. Mater.* **2003**, *15*, 1438−1442.

(8) Kang, Y. X.; Bai, Y.; Fan, W.; Yuan, T.; Gao, Y.; Bao, C. G.; Li, B. Q. Thermal cycling performance of $La_2Ce_2O_7$/50 vol.% YSZ composite thermal barrier coating with CMAS corrosion. *J. Eur. Ceram. Soc.* **2018**, *38*, 2851−2862.

(9) Pizzolitto, C.; Menegazzo, F.; Ghedini, E.; Innocenti, G.; Di Michele, A.; Cruciani, G.; Cavani, F.; Signoretto, M. Increase of Ceria Redox Ability by Lanthanum Addition on Ni Based Catalysts for Hydrogen Production. *ACS Sustainable Chem. Eng.* **2018**, *6*, 13867−13876.

(10) Weng, S. F.; Wang, Y. H.; Lee, C. S. Autothermal steam reforming of etanol over $La_2Ce_{2-x}Ru_xO_7$ (x = 0−0.35) catalyst for hydrogen production. *Appl. Catal., B* **2013**, *134-135*, 359−366.

(11) Zhu, Z.; Sun, W.; Wang, Z.; Cao, J.; Dong, Y.; Liu, W. A high stability Ni-$La_{0.5}Ce_{0.5}O_{2-\delta}$ asymmetrical metal-ceramic membrane for hydrogen separation and generation. *J. Power Sources* **2015**, *281*, 417−424.

(12) Zhao, J.; Xu, X.; Zhou, W.; Blakey, I.; Liu, S.; Zhu, Z. Proton-conducting La-doped ceria-based internal reforming layer for direct methane solid oxide fuel cells. *ACS Appl. Mater. Interfaces* **2017**, *9*, 33758−33765.

(13) Kochetova, N.; Animitsa, I.; Medvedev, D.; Demin, A.; Tsiakaras, P. Recent activity in the development of proton-conducting oxides for high-temperature applications. *RSC Adv.* **2016**, *6*, 73222−73268.

(14) Besikiotis, V.; Knee, C.; Ahmed, I.; Haugsrud, R.; Norby, T. Crystal structure, hydration and ionic conductivity of the inherently oxygen-deficient $La_2Ce_2O_7$. *Solid State Ionics* **2012**, *228*, 1−7.

(15) Lucid, A. K.; Keating, P. R. L.; Allen, J. P.; Watson, G. W. Structure and Reducibility of CeO_2 Doped with Trivalent Cations. *J. Phys. Chem. C* **2016**, *120*, 23430−23440.

(16) Sun, Q.; Fu, Z.; Yang, Z. Effects of rare-earth doping on the ionic conduction of CeO_2 in solid oxide fuel cells. *Ceram. Int.* **2018**, *44*, 3707−3711.

(17) Tinwala, H.; Shah, P.; Siddhapara, K.; Shah, D.; Menghani, J. Investigation of ionic conductivity of lanthanum cerium oxide nano crystalline powder synthesized by co precipitation method. *J. Cryst. Growth* **2016**, *452*, 54−56.

(18) Mogensen, M.; Sammes, N. M.; Tompsett, G. A. Physical, chemical and electrochemical properties of pure and doped ceria. *Solid State Ionics* **2000**, *129*, 63−94.

(19) Minervini, L.; Zacate, M. O.; Grimes, R. W. Defect cluster formation in M_2O_3-doped CeO_2. *Solid State Ionics* **1999**, *116*, 339−349.

(20) Steele, B. C. H. Materials for IT-SOFC stacks: 35 years R&D: the inevitability of gradualness? *Solid State Ionics* **2000**, *134*, 3−20.

(21) Artini, C.; Pani, M.; Carnasciali, M. M.; Buscaglia, M. T.; Plaisier, J. R.; Costa, G. A. Structural Features of Sm- and Gd-Doped Ceria Studied by Synchrotron X-ray Diffraction and μ-Raman Spectroscopy. *Inorg. Chem.* **2015**, *54*, 4126−4137.

(22) Artini, C.; Pani, M.; Lausi, A.; Masini, R.; Costa, G. A. High temperature structural study of Gd- doped ceria by synchrotron X-ray diffraction (673 K ≤ T ≤ 1073 K). *Inorg. Chem.* **2014**, *53*, 10140−10149.

(23) Suda, E.; Pacaud, B.; Mori, M. Sintering characteristics, electrical conductivity and thermal properties of La-doped ceria powders. *J. Alloys Compd.* **2006**, *408*−*412*, 1161−1164.

(24) Wang, L. S.; Li, C. X.; Li, C. J.; Yang, C. J. Performance of $La_{0.8}Sr_{0.2}Ga_{0.8}Mg_{0.2}O_3$-based SOFCs with atmospheric plasma sprayed La-doped CeO_2 buffer layer. *Electrochim. Acta* **2018**, *275*, 208−217.

(25) Hong, J. E.; Ida, S.; Ishihara, T. Effects of transition metal addition on sintering and electrical conductivity of La-doped CeO_2 as buffer layer for doped $LaGaO_3$ electrolyte film. *Solid State Ionics* **2014**, *262*, 374−377.

(26) Zhu, Z.; Liu, B.; Shen, J.; Lou, Y.; Ji, Y. $La_2Ce_2O_7$: A promising proton ceramic conductor in hydrogen economy. *J. Alloys Compd.* **2016**, *659*, 232−239.

DOI: 10.1021/acs.inorgchem.9b01104
Inorg. Chem. 2019, 58, 9368−9377

(27) Tu, T.; Zhang, B.; Liu, J.; Wu, K.; Peng, K. Synthesis and conductivity behaviour of Mo-doped $La_2Ce_2O_7$ proton conductors. *Electrochim. Acta* **2018**, *283*, 1366−1374.
(28) Zhang, B.; Zhong, Z.; Tu, T.; Wu, K.; Peng, K. Acceptor-doped $La_{1.9}M_{0.1}Ce_2O_7$ (M = Nd, Sm, Dy, Y, In) proton ceramics and in-situ formed electron-blocking layer for solid oxide fuel cells applications. *J. Power Sources* **2019**, *412*, 631−639.
(29) Vanpoucke, D. E. P.; Bultinck, P.; Cottenier, S.; Van Speybroeck, V.; Van Driessche, I. Density functional theory study of $La_2Ce_2O_7$: disordered fluorite versus pyrochlore structure. *Phys. Rev. B: Condens. Matter Mater. Phys.* **2011**, *84*, 054110.
(30) Zhang, Q.; Zheng, X.; Jiang, J.; Liu, W. Structural stability of $La_2Ce_2O_7$ as a proton conductor: a first-principles study. *J. Phys. Chem. C* **2013**, *117*, 20379−20386.
(31) Reynolds, E.; Blanchard, P. E. R.; Zhou, Q.; Kennedy, B. J.; Zhang, Z.; Jang, L. J. Structural and spectroscopic studies of $La_2Ce_2O_7$: disordered fluorite versus pyrochlore structure. *Phys. Rev. B: Condens. Matter Mater. Phys.* **2012**, *85*, 132101.
(32) Bae, J. S.; Choo, W. K.; Lee, C. H. The crystal structure of ionic conductor $La_xCe_{1-x}O_{2-x/2}$. *J. Eur. Ceram. Soc.* **2004**, *24*, 1291−1294.
(33) Amsif, M.; Marrero-López, D.; Magrasó, A.; Peña-Martínez, J.; Ruiz-Morales, J. C.; Núñez, P. Synthesis and characterisation of $BaCeO_3$-based proton conductors obtained from freeze-dried precursors. *J. Eur. Ceram. Soc.* **2009**, *29*, 131−138.
(34) Dos Santos-Gómez, L.; Compana, J. M.; Bruque, S.; Losilla, E. R.; Marrero-López, D. Symmetric electrodes for solid oxide fuel cells based on Zr-doped $SrFeO_{3-\delta}$. *J. Power Sources* **2015**, *279*, 419−427.
(35) *PANalytical X'Pert HighScore Plus Suite, B. V.*, Lelyweg 1, 7602 EA Almelo, The Netherlands, 2014.
(36) Larson, A. C.; von Dreele, R. B. *General Structure Analysis System (GSAS)*; Los Alamos National Laboratory, 1994.
(37) Abrantes, J. C. C. *Estereologia, UIDM, ESTG*; Polytechnic Institute of Viana do Castelo, Viana do Castelo, Portugal, 1998.
(38) Andrievskaya, E. R.; Kornienko, O. A.; Sameljuk, A. V.; Sayir, A. Phase relation studies in the CeO_2−La_2O_3 system at 1100−1500 °C. *J. Eur. Ceram. Soc.* **2011**, *31*, 1277−1283.
(39) Yamamura, H.; Nishino, H.; Kakinuma, K.; Nomura, K. Crystal Phase and Electrical Conductivity in the Pyrochlore-Type Composition Systems, $Ln_2Ce_2O_7$ (Ln = La, Nd, Sm, Eu, Gd, Y and Yb). *J. Ceram. Soc. Jpn.* **2003**, *111*, 902−906.
(40) Kalland, L. E.; Norberg, S. T.; Kyrklund, J.; Hull, S.; Eriksson, S. G.; Norby, T.; Mohn, C. E.; Knee, C. S. C-type related order in the defective fluorites $La_2Ce_2O_7$ and $Nd_2Ce_2O_7$ studied by neutron scattering and ab initio MD simulations. *Phys. Chem. Chem. Phys.* **2016**, *18*, 24070−24080.
(41) Coduri, M.; Scavini, M.; Allieta, M.; Brunelli, M.; Ferrero, C. Defect Structure of Y-Doped Ceria on Different Length Scales. *Chem. Mater.* **2013**, *25*, 4278−4289.
(42) López-Vergara, A.; Porras-Vázquez, J. M.; Infantes-Molina, A.; Canales-Vázquez, J.; Cabeza, A.; Losilla, E. R.; Marrero-López, D. Effect of Preparation Conditions on the Polymorphism and Transport Properties of $La_{6-x}MoO_{12-\delta}$ ($0 \leq x \leq 0.8$). *Chem. Mater.* **2017**, *29*, 6966−6975.
(43) Handal, H. T.; Thangadurai, V. Evaluation of chemical stability, thermal expansion coefficient, and electrical properties of solid state and wet-chemical synthesized Y and Mn-codoped CeO_2 for solid oxide fuel cells. *J. Power Sources* **2013**, *243*, 458−471.
(44) Wallenberg, R.; Withers, R.; Bevan, D. J. M.; Thompson, J. G.; Barlow, P.; Hyde, B. G. The fluorite-related "solid solutions" of CeO_2-Y_2O_3 I: A re-examination by electron microscopy and diffraction. *J. Less-Common Met.* **1989**, *156*, 1−16.
(45) McBride, J. R.; Hass, K. C.; Poindexter, B. D.; Weber, W. H. Raman and x-ray studies of $Ce_{1-x}RE_xO_{2-y}$, where RE = La, Pr, Nd, Eu, Gd, and Tb. *J. Appl. Phys.* **1994**, *76*, 2435.
(46) Ohashi, T.; Yamazaki, S.; Tokunagaa, T.; Arita, Y.; Matsui, T.; Harami, T.; Kobayashi, K. EXAFS study of $Ce_{1-x}Gd_xO_{2-x/2}$. *Solid State Ionics* **1998**, *113*−*115*, 559−564.
(47) Mandal, B. P.; Grover, V.; Roy, M.; Tyagi, A. K. X-Ray Diffraction and Raman Spectroscopic Investigation on the Phase Relations in Yb_2O_3- and Tm_2O_3-Substituted CeO_2. *J. Am. Ceram. Soc.* **2007**, *90*, 2961−2965.
(48) Nakajima, A.; Yoshihara, A.; Ishigame, M. Defect-induced Raman spectra in doped CeO_2-Gd_2O_3 solid solutions. *Phys. Rev. B: Condens. Matter Mater. Phys.* **1994**, *50*, 13297−13307.
(49) Horlait, D.; Claparède, L.; Clavier, N.; Szenknect, S.; Dacheux, N.; Ravaux, J.; Podor, R. Stability and Structural Evolution of $Ce^{IV}_{1-x}Ln^{III}_xO_{2-x/2}$ Solid Solutions: A Coupled μ-Raman/XRD Approach. *Inorg. Chem.* **2011**, *50*, 7150−7161.
(50) Presto, S.; Artini, C.; Pani, M.; Carnaciali, M. M.; Massardo, S.; Viviani, M. Ionic conductivity and local structure features in $Ce_{1-x}Sm_xO_{2-x/2}$. *J. Phys. Chem. Phys.* **2018**, *20*, 28338−28345.
(51) Li, J. G.; Ikegami, T.; Mori, T. Low temperature processing of dense Samarium-doped CeO_2 ceramics: sintering and grain growth behaviors. *Acta Mater.* **2004**, *52*, 2221−2228.
(52) Abrantes, J. C. C.; Labrincha, J. A.; Frade, J. R. Applicability of the brick layer model to describe the grain boundary properties of strontium titanate ceramics. *J. Eur. Ceram. Soc.* **2000**, *20*, 1603−1609.
(53) Marrero-López, D.; Ruiz-Morales, J. C.; Peña-Martínez, J.; Martín-Sedeño, M. C.; Ramos-Barrado, J. R. Influence of phase segregation on the bulk and grain boundary conductivity of LSGM electrolytes. *Solid State Ionics* **2011**, *186*, 44−52.
(54) Irvine, J. T. S.; Sinclair, D. C.; West, A. R. Electroceramics: characterization by impedance spectroscopy. *Adv. Mater.* **1990**, *2*, 132−138.
(55) Kilner, J. A. Fast oxygen transport in acceptor doped oxides. *Solid State Ionics* **2000**, *129*, 13−23.
(56) Tianshu, Z.; Hing, P.; Huang, H.; Kilner, J. Ionic conductivity in the CeO_2−Gd_2O_3 system ($0.05 \leq Gd/Ce \leq 0.4$) prepared by oxalate coprecipitation. *Solid State Ionics* **2002**, *148*, 567−573.
(57) Pérez-Coll, D.; Marrero-López, D.; Núñez, P.; Piñol, S.; Frade, J. R. Grain boundary conductivity of $Ce_{0.8}Ln_{0.2}O_{2-\delta}$ ceramics (Ln = Y, La, Gd, Sm) with and without Co-doping. *Electrochim. Acta* **2006**, *51*, 6463−6469.
(58) Nigara, Y.; Kawamura, K.; Kawada, T.; Mizusaki, J. Hydrogen permeability in $Ce_{0.8}Yb_{0.2}O_{1.9}$ at high temperatures. *Solid State Ionics* **2000**, *136*−*137*, 215−221.
(59) Kim, S.; Anselmi-Tamburini, U.; Park, H. J.; Martin, M.; Munir, Z. A. Unprecedented Room-Temperature Electrical Power Generation Using Nanoscale Fluorite-Structured Oxide Electrolytes. *Adv. Mater.* **2008**, *20*, 556−559.
(60) Shipour, M.; Gregori, G.; Merkle, R.; Maier, J. On the proton conductivity in pure and gadolinium doped nanocrystalline cerium oxide. *Phys. Chem. Chem. Phys.* **2011**, *13*, 937−940.
(61) Tandé, C.; Pérez-Coll, D.; Mather, G. L. Surface proton conductivity of dense nanocrystalline YSZ. *J. Mater. Chem.* **2012**, *22*, 11208.
(62) Pérez-Coll, D.; Marrero-López, D.; Ruiz-Morales, J. C.; Núñez, P.; Abrantes, J. C.; Frade, J. R. Reducibility of $Ce_{1-x}Gd_xO_{2-\delta}$ in prospective working conditions. *J. Power Sources* **2007**, *173*, 291−297.
(63) Tao, Z.; Bi, L.; Fang, S.; Liu, W. A stable $La_{1.95}Ca_{0.05}Ce_2O_{7-\delta}$ as the electrolyte for intermediate-temperature solid oxide fuel cells. *J. Power Sources* **2011**, *196*, 5840−5843.

DOI: 10.1021/acs.inorgchem.9b01104
Inorg. Chem. 2019, 58, 9368−9377